Investigation of unsteady surface pressure aerodynamics over a two-wheeled landing gear model

A. Gatto[1]
Brunel University London, Uxbridge, England, UB8 3PH, United Kingdom

and
W. R. Graham[2]
University of Cambridge, Cambridge, England, CB2 1PZ, United Kingdom

Unsteady flow around deployed landing gears is a significant contributor to aircraft noise on approach. The far-field sound is largely determined by the fluctuating pressures on the gear surface, quantities which have yet to be fully characterized even for simplified representations. The current work reports axle- and wheel-surface data from a comprehensive set of measurements on a generic, two-wheel, landing-gear model. The results show the expected high levels of unsteadiness on areas exposed to large-scale separated flow, of which some (wheel rear surfaces and forward edges) can be identified from steady data, but others (wheel faces adjacent to axle wakes, flow impingements on sidewalls) cannot. The forward-edge values for the current, untripped, configuration are markedly greater than previously reported measurements with artificial transition fixing. Spectral analysis highlights a further category of potentially important contributions that are not easily detected in overall RMS values: high-frequency unsteadiness associated with turbulent attached, or attaching, flows. A key implication of these results is the need for accurate representation of the true, full-scale, boundary-layer state in computations and model-scale testing.

Nomenclature

C_p = pressure coefficient

D = wheel diameter, m

W = maximum width of landing gear , m

L = length of main support strut to wheel axle, m

A = amplitude

θ = wheel rotation angle, deg

R = reference (as subscript)

[1]Senior Lecturer in Aerospace Engineering, Aerospace Division, Dept. of Mechanical, Aerospace, and Civil Engineering. Senior Member AIAA.
[2]Senior Lecturer, Department of Engineering. Member AIAA.

I. Introduction

A significant proportion of the noise from modern aircraft on landing comes from airframe components [1,2]. Of these, one of the most dominant is the landing gear [1]. The complex, unsteady flow around this bluff structure gives rise to strong aeroacoustic sources, whose characteristics are not yet well enough understood to reliably inform low-noise design.

Initial research on the topic was generally restricted to experimental noise measurements. These allowed identification of fundamental features — cavity-related tones and a 'velocity-to-the-sixth-power' broadband component [3] — as well as empirical investigation of possible modifications [4–8]. However, for detailed characterisation of the problem, local flow-field information is essential. In particular, the unsteady pressures on the gear surfaces are unquestionably crucial to noise generation, and the surrounding turbulent flow may contribute too [9,10]. Mean-flow features are also important, insofar as they allow the locations of significant noise-generating regions to be inferred.

Early recognition of the need for local information is evident in the targeted surface pressure measurements of Heller and Dobrzynski [11], and the mean-flow experiments carried out by Lazos [12,13]. More extensive datasets have followed, from both two-wheel [9,10,14–19] and four-wheel [20] models. Associated with these measurements have been significant computational efforts, intended to validate and develop calculation capabilities for the local flow field [9,10,15-19,23] and the radiated sound [9,10,16-19]. While the results represent impressive progress on both fronts, they also demonstrate that reliable, independent, prediction of the unsteady surface pressures cannot yet be guaranteed. Experimental characterization of these quantities is therefore still necessary.

Venkatakrishnan et al's four-wheel-model tests [20] included unsteady pressure measurements over the wheel surfaces and at a number of other locations. However, although the RMS levels on the wheels have been reported by Spalart and Mejia [21], a spectral analysis seems not to be publicly available. Similar information for a two-wheel gear is also sparse; results in [19] are restricted to steady data, while only a subset of the pressure measurements on the LAGOON model considered in [9,10,14–18] included fluctuating components.

Knowledge of the local flow quantity most directly related to landing-gear noise thus remains incomplete. The current work aims to address this issue. To this end, unconventional use is made of multiple, low-cost, miniature dynamic pressure transducers to map the surface pressure field on a simplified, quarter-scale, two-wheel landing-gear model.

This paper reports the results for the wheel and axle surfaces. Section II describes the experimental approach. The results are presented and discussed in Section III, considering first steady flow features, and then the unsteady pressures in both RMS and spectral form. The conclusions are summarized in Section IV.

II. Experimental Setup and Apparatus

A. The landing gear model

A schematic of the experimental model is shown in Fig. 1. The model is an idealized quarter-scale (D = 0.36m, W = 0.5m, L = 0.69m) representation of a two-wheeled landing gear, incorporating shallow wheel-cavity detail as well as a near-realistic wheel profile. Its main structural support strut is surrounded by an outer shroud, which contains nine planes of pressure sensors distributed along its length. Each plane has five sensors spaced at 60° intervals, and the shroud is manually rotatable by up to ±40°. A yaw adjustment plate (range ±20°) and a six-axis load cell complete the model structure.

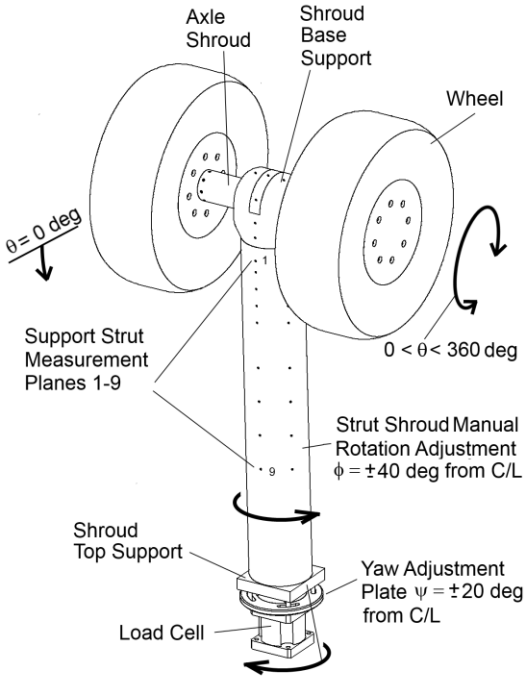

Fig 1. Schematic of the wind tunnel model, showing overall functionality.

Further instrumentation is installed in the shroud base support, axle shroud and wheels, as shown in Fig. 2. Some of the sensors in the base support (0–8) are further designated ‘F’, ‘B’ or ‘S’, signifying position on the front, back, or side respectively. The remaining 46 transducers are distributed along the axle shroud and wheels in a single plane, with spacings chosen to maximize resolution, subject to practical constraints and the degree of expected spatial

variation. Each is embedded in a 4mm diameter internal cavity a short distance (typically less than 2mm) behind a 0.8mm surface orifice. The typical distance from model surface to transducer diaphragm is 3.5mm, ensuring negligible resonance and lag effects.

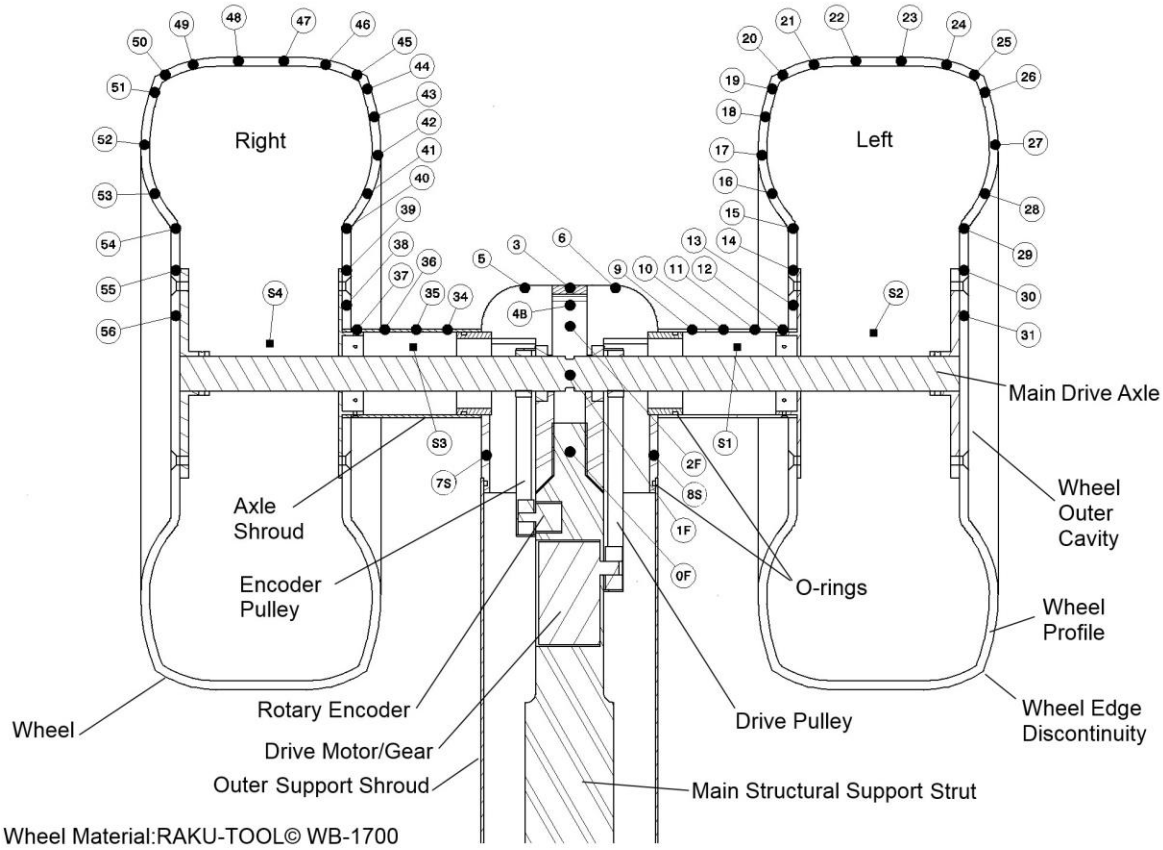

Fig 2. Internal structure and pressure-sensor placement for landing-gear test model(front view).

Full-surface mapping capability is achieved via a 1:1200 DC motor/gearbox assembly connected to the axle with a drive pulley. This allows the wheels and axle shroud to be rotated through 360°, with position monitored by a rotary encoder (Baumer BTIV 24S). A software-based integrated PID controller is used to set and maintain wheel angle during testing.

To facilitate the manual rotation adjustment of the strut shroud, embedded O-rings are installed in the top and base supports (the latter near sensors 7S and 8S, as indicated on Fig. 2). Similar O-rings are also used for the axle shrouds (near transducers 9 and 34). These joints ensure an airtight seal, thereby providing a constant and uniform static pressure within the model under test conditions. This is a crucial design feature, as the transducer measurements are referenced to the internal pressure. Several additional pressure sensors, distributed throughout the internal cavities (cf., for example, S1–S4 in Fig. 2) are used to monitor this pressure. These transducers are

referenced, via pneumatic tubes, to atmospheric conditions outside the wind tunnel. Measurements during operation confirmed uniformity, with no significant difference from the ambient value. Offset corrections were therefore not applied.

B. Pressure transducer calibration.

Honeywell CPC03GFH pressure transducers were used for all measurements. These active strain-gauge/diaphragm sensors have a cylindrical measurement port and connections for PCB mounting. A custom-designed miniature PCB was integrated onto each transducer to provide signal amplification and conditioning electronics. The resulting devices have: (1) small overall dimensions (20mm x 10mm x 7mm), allowing access to areas within the model where space is limited; (2) low capital cost compared to the industry-standard Kulite© sensors used in similar studies [14,15,20]; and (3) relatively flat response characteristics over the frequency range of interest, including the DC limit.

Each transducer was calibrated in a purpose-built rig, consisting of an evacuated chamber 25mm in length and diameter, with the facility to mount the transducer opposite a Bruel & Kjaer, laboratory-standard, 4180 reference microphone. To obtain the mean calibration, a manual pressurization port on the back of the chamber was used, with a Digitron 2081P pressure meter fitted in place of the microphone. From these mean-pressure calibration tests, typical maximum deviations within a 95% confidence interval were found to be less than ±5% of full-scale output. To assess the dynamic performance of each sensor, a generic 50mm-diameter loudspeaker was mounted directly to the front of the chamber and driven with white noise. The resulting transducer and microphone signals were then used to obtain the transducer response over the 0–6kHz frequency range.

The result of a typical calibration is shown in Fig. 3. The transducer response is near flat up to approximately 2.5kHz. From here to 3.1kHz, a reduction in amplitude ratio is observed before a significant increase up to resonance at 4.25kHz (±0.25kHz for the transducer ensemble). While it was found possible to correct for this phenomenon with reasonable accuracy up to 5kHz, to minimize complexity, data acquisition time, and errors an upper frequency limit of 3.5kHz was chosen. (Maximum amplitude variation of any one transducer was within ±1.8dB at 3.5kHz.)

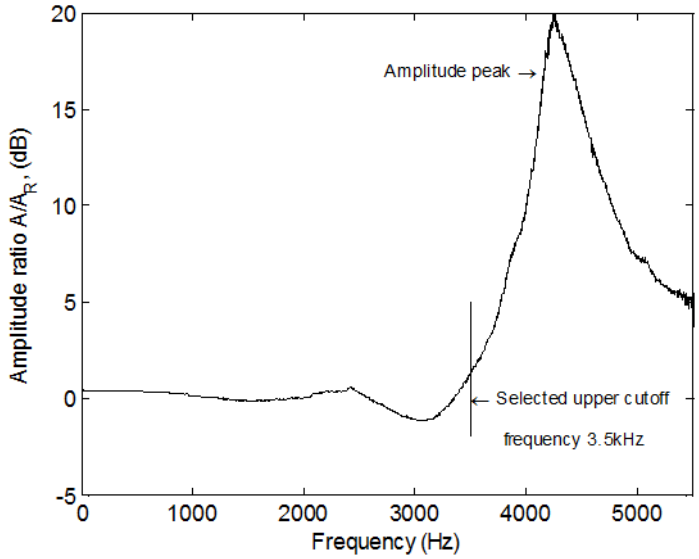

Fig 3. Typical frequency response characteristics for the pressure transducers.

C. Wind tunnel test environment and procedure

The model was tested in the Markham wind tunnel at the University of Cambridge. This is a closed-circuit tunnel, with a maximum flow velocity of 60m/s and a closed test section of size 1.68m x1.22m (giving a model blockage, based on frontal area, of 7.5%). The turbulence level is 0.2%. The operating flow speed was 30m/s, corresponding to a Reynolds number (based on wheel diameter) of 7.4×10^5.

The model was mounted on a support under the tunnel floor, with a two-piece, flat-plate aluminum cover placed over the exposed opening to minimize aerodynamic disturbance. A nominal 5mm gap between the support strut and the cover was provided to ensure unhindered model deflection under aerodynamic loading. Each model configuration was tested in a block of three separate wind-tunnel runs, with the strut shroud rotated 20° between each. A given run encompassed a complete rotation from $\theta = 0°$ to 360° (in 20° steps), which was then reversed to unwind the internal sensor cables.

The need for artificial transition fixing in model-scale landing-gear testing remains uncertain. Although boundary-layer trips were employed on the LAGOON [14] and 'rudimentary landing gear' [20] models, this was primarily to ensure 'CFD-friendliness' for validation purposes. Indeed, given the bluff nature of a landing gear, one would expect the state of the boundary-layer to be largely determined by the separations and reattachments that the geometry imposes. Here, therefore, no trips were installed.

Measurement signals were sampled by two linked National Instruments USB-6255 data acquisition and controller boards, after passing through purpose-built 8th-order, elliptical, low-pass integrated-circuit filters. The cut-off frequency was controlled by a single USB-6255 analog output channel generating a TTL square wave with nominal frequency one hundred times the desired cut-off value (which was set to 5.5kHz). The filtered signals were sampled at 12kHz for 10s. One of the USB-6255 boards was also used to control wheel/axle rotation, via an H-bridge motor-driver integrated circuit connected to the motor/gearbox unit. Before and after every run, a zero, wind-off, data point was taken. This allowed compensation for any thermal drift of measurement zeros during the experiment, as well as identification of superfluous, non-aerodynamic, frequency components in the data collected.

III. Results and Discussion

For reasons of length, this paper focuses on the pressure measurements over the wheel and axle areas. First (Section IIIA), mean wheel center-line pressures are compared against previous work. Then the dataset is considered in its entirety, in terms of its mean (Section IIIB) and fluctuating (Sections IIIC and D) components. Throughout, measurement locations are denoted by 'PT', followed by the transducer number (cf. Fig. 2).

A. Validation of the Baseline Flow Field

Figure 4 shows a comparison of the mean pressure distributions measured at PT22 and PT47 with center-line values reported, for a similar two-wheel gear, in [19]. The agreement is excellent, particularly in light of the differing Reynolds Numbers: 1.8×10^6 in [19] compared to 7.4×10^5 here (hence also providing a degree of support for the dominance of body geometry over Reynolds-number influence argued for above). The greatest difference is observed at $\theta = 200°$, where the suction pressure is higher than in [19]. The reason for this discrepancy is not known; however, the result is consistent across wheels, suggesting that it is genuine. Indeed, the measurements show excellent agreement between wheels, confirming that the expected zero-yaw flow symmetry was near achieved.

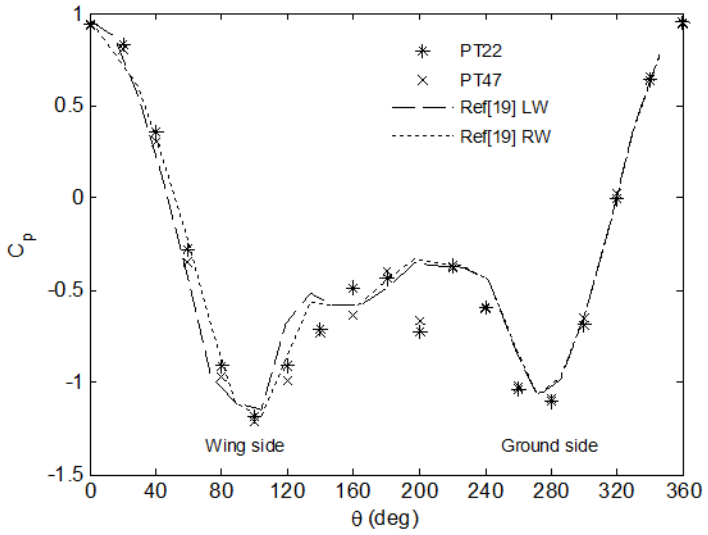

Fig. 4. Comparison of mean pressure distributions on wheels with available literature.

Wheel static pressure distributions have also been reported for the LAGOON model [15]. These agree qualitatively with those in Fig. 4, but show lower peak suction levels, with pressure-coefficient values around –0.95 and –0.75 on the wing and ground sides respectively. The difference almost certainly arises from wheel geometry; while the dimensions used here match (proportionally) those in [19], the LAGOON model's wheels are not only narrower, but also have deep cavities on their inner sides.

B. Mean Pressure Distributions

Figure 5 shows iso-contours of mean pressure coefficient over the wheels and axles. It is immediately apparent that the strong wheel-to-wheel correspondence noted for the center-line distributions is representative of general agreement in the pressure fields as a whole.

Viewed from upstream (Fig. 5a), the pressures show the expected maxima in the stagnation regions associated with flow impingement on the wheels (A) and axles (C). The former are located slightly inboard of the wheel center line, due to deflection of the oncoming flow in the outboard direction. This behavior is also seen on the front wheels of four-wheel gears [13]; in that context, it has been ascribed to the presence of the support truck [20]. Here, the flow obstruction from the axle and strut has the same effect. As a result, the suction over the outboard leading edges (B) is significantly higher than over those inboard. The subsequent adverse pressure gradient leads to flow separation, followed by transition and reattachment, as indicated by the oil flow in Fig. 6 and previously observed by Lazos [13]. Tripping the boundary layer on the front face has been found to eliminate this separation bubble [20].

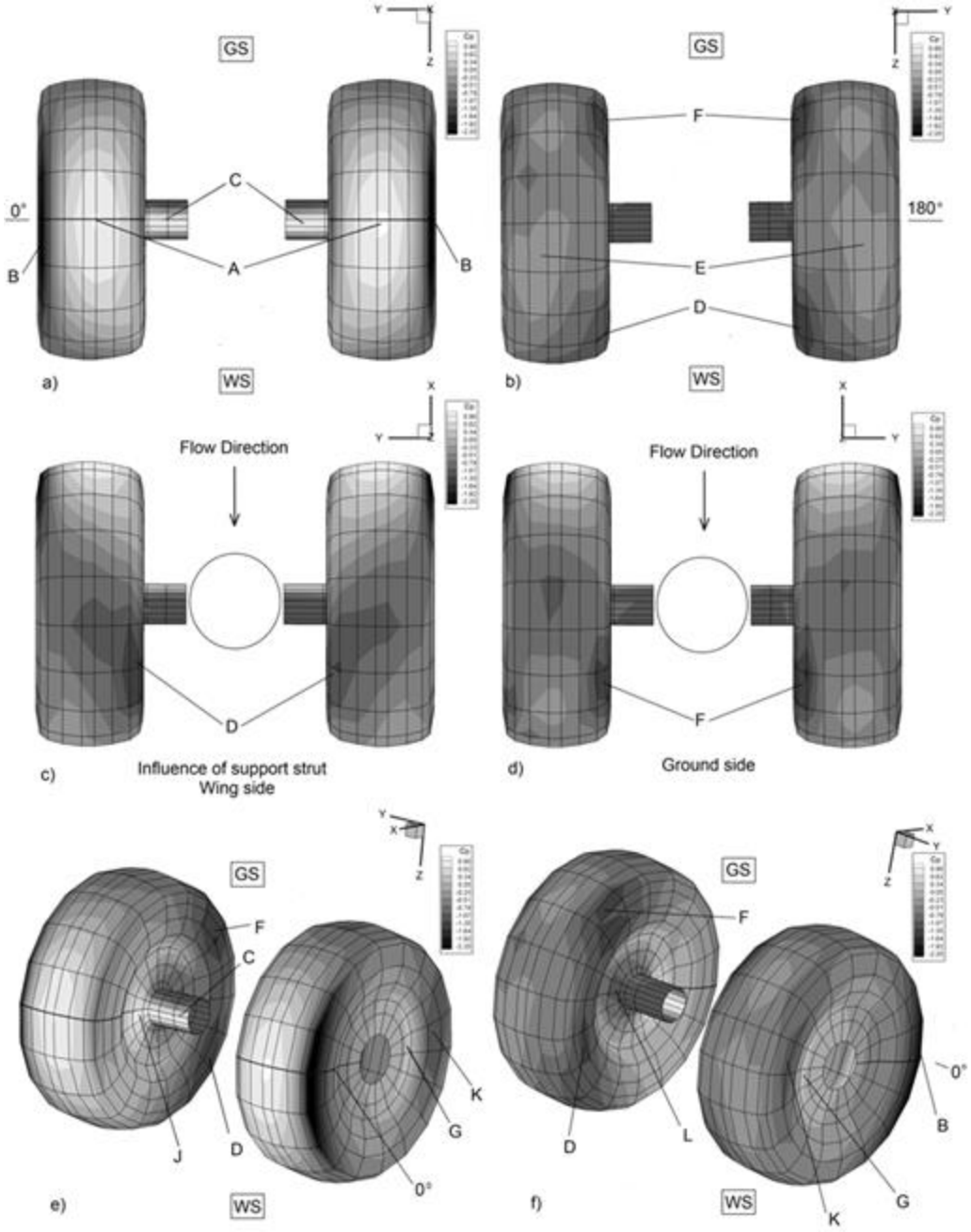

Fig. 5. Iso-contours of mean pressure distributions over the wheel and axle assemblies.

A less evident departure from symmetry is manifested by a slight displacement (of about 20°) of the axle stagnation region towards the wing side, due to the blocking effect of the strut. Again, this is in qualitative agreement with four-wheel model experiments [20]. Its presence can also be inferred for the LAGOON model from the axle pressure-coefficient value — 0.74, well below stagnation — in the directly upstream position [18]. (For comparison, PT11 here measures 0.76 at the same location.)

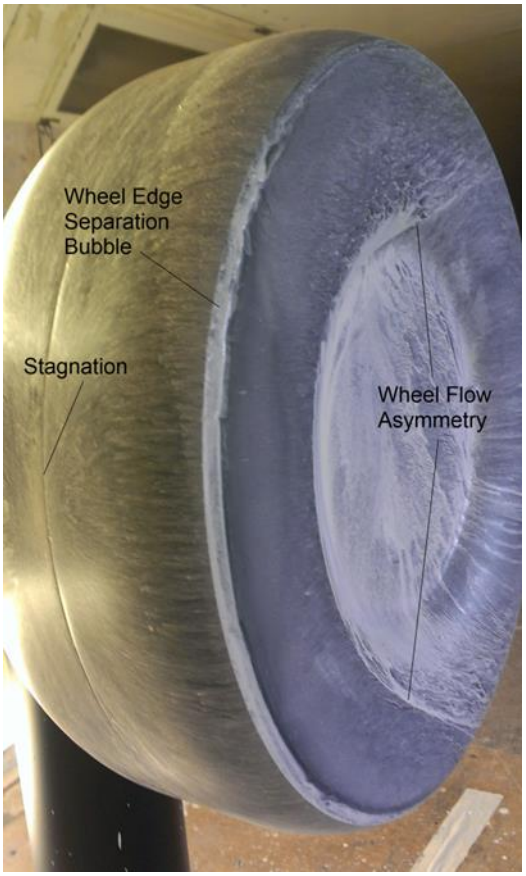

Fig. 6. Oil flow visualization over the left wheel (flow from left to right).

The asymmetry is more obvious in the view of the pressure field from downstream (Fig. 5b). Here the lowest pressures are found on the inboard edges (regions F and D), as the flows from the inner faces swirl into the wheel wakes. Their confluences with counterparts from the outer faces lead to areas of higher pressure, of which E, on the wing side, is the most dominant. Between E and the corresponding ground-side region is the low-pressure dip noted in the profiles of Fig. 4, which is now seen to be compatible with a physical description of the wheel flow. The downstream-edge features observed here are consistent with those found on the front wheels of four-wheel models [13,20], and on a single wheel [22]. However, unsurprisingly, the overall field differs somewhat in detail.

A clearer comparison of the downstream-edge suction regions is available from Figs. 5c and 5d, which show the pressure field viewed along the strut axis, from wing and ground sides respectively. The presence of the strut is associated with a much more extensive area of low pressure, presumably due to higher local flow speeds. More generally, the pressure field exhibits greater uniformity across the wheel surface on the (strut-free) ground side.

Figures 5e and 5f show perspective views of the surface pressures from upstream and downstream. This allows the effect of the axle on the inner wheel faces — higher pressure upstream (J) and wake influence downstream (L)

— to be seen. Also visible are variations associated with the outer-face profile geometry, in particular a higher-pressure area (G) due to flow impingement on the sloping part, followed by lower pressure (K) as the fluid accelerates around the sidewall bulge.

C. RMS Pressure Distributions

Prior to calculating the unsteady RMS pressure values, all sampled data was post-processed through a 7^{th} order elliptical digital filter with a 50dB stopband attenuation. The cut-off frequency for this filter was set at the chosen upper-limit value, 3.5kHz (cf. Section IIIB).

The distribution of RMS pressure on the wheels and axles is shown, in pressure-coefficient form, in Fig. 7. Broadly, these results support Lazos' contention [12] that characterization and understanding of mean-flow features is a useful initial step towards noise prediction. Specifically, the regions of high unsteadiness tend to be associated with separation, whereas attached flow (either laminar or turbulent) leads to much lower levels. Thus the stagnation regions (denoted 'A' in Fig. 7a) exhibit negligible pressure unsteadiness, while portions of the wheels below the rear-face vortices (D, E and F) show strong activity, as do the localized separation-bubble arcs (B). Less evidently deducible from the steady results, but still to be expected, is an 80° wedge (G) due to the axle wake, whose influence remains visible even on the rear faces (C). This feature contains some of the highest measured magnitudes (e.g. 0.3, for PT19 at $\theta = 160°$).

Nonetheless, there are some more subtle features that might not be anticipated from the mean pressure data. Immediately behind the axle, and before its wake impinges, there are clear shear-layer 'footprints' (H), corresponding to the expected leg positions of the axle horseshoe vortex identified by Lazos [12]. Less marked are slightly raised levels at J and K (cf. Figs. 7e and 7f), which can be ascribed to impingement of weak shear layers over the wheel cavities. Support for this claim comes from Fig. 6, with the oil flow visualization suggesting that the cavity fluid is more-or-less stagnant, despite there being little indication of separation in the steady pressure field.

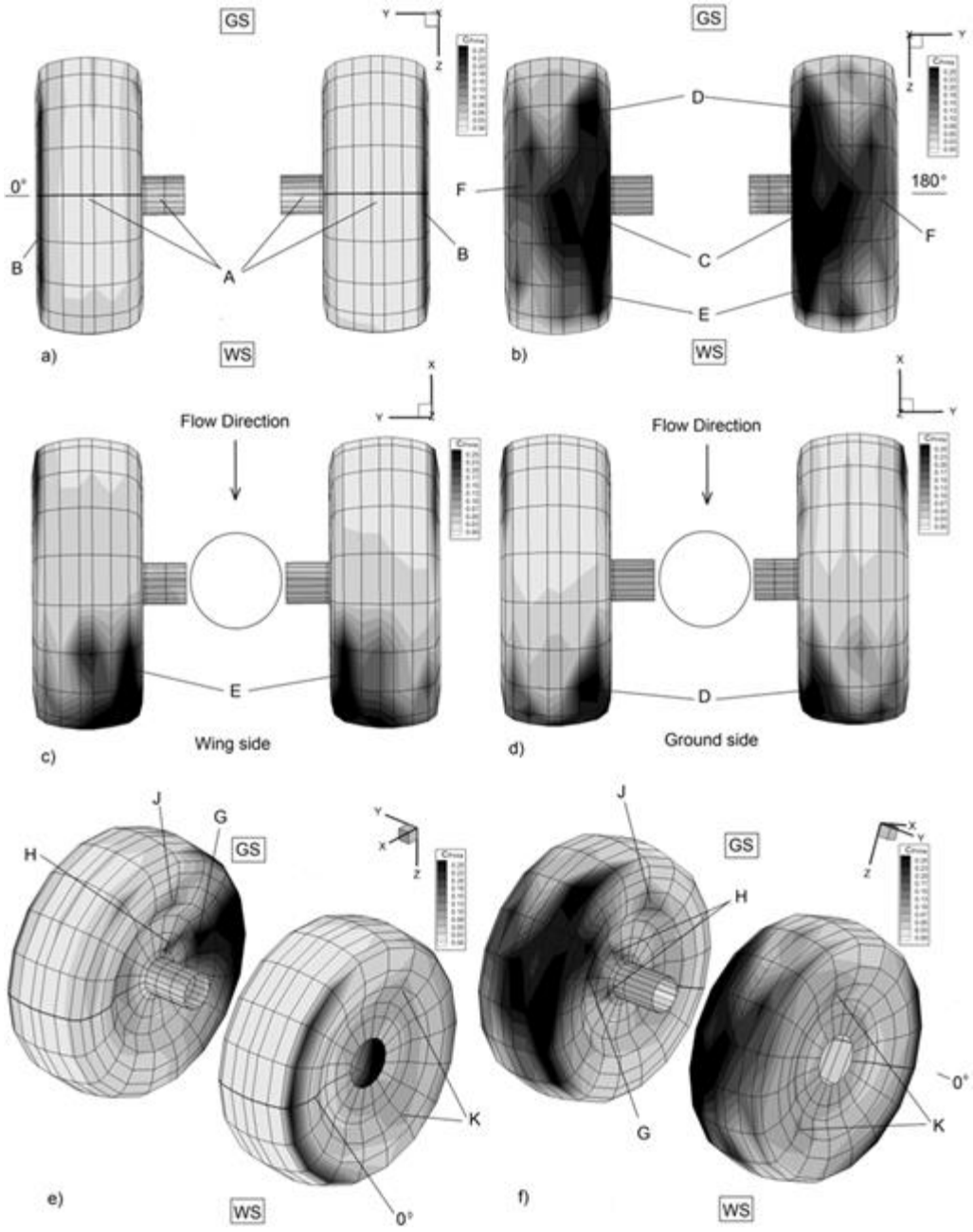

Fig. 7. RMS pressure distributions over the wheel and axle assemblies.

Elsewhere in the literature, extensive unsteady surface pressure distributions have only been reported for a four-wheel model [21,23], so comparisons are necessarily qualitative. The range of levels shown by Xiao et al [23] is in good agreement with the values seen in the current data. However, the leading-edge measurement (estimated from the color map in [21]) is only about one-third of that found here, presumably thanks mainly to the elimination of the separation bubble by prior boundary-layer tripping. (A geometry effect is also to be expected, as the four-wheel model has significantly greater edge radii.) This implies that, while Reynolds-number effects may be relatively

unimportant for the mean flow, they are potentially significant for the unsteady component. Hence knowledge of the true boundary-layer state on full-size gears in operation may be important for accurate noise prediction.

D. Spectral Analysis

More detailed insight into the unsteady surface pressure measurements is provided by their power spectral densities. The presentation is separated into four sub-sections describing: the axle region; the inner wheel surface; the tire belt; and the outer wheel surface. Since flow symmetry has been inferred, only data for the right axle/wheel combination is presented. All spectra are plotted over a frequency range 10Hz to 2kHz, with each result being obtained from the average of 39 time segments of 0.5s, using a Hanning window with 50% overlap. Direct, quantitative, assessment against previously published data is complicated by scaling effects in both amplitude and frequency, but qualitative comparisons are made where possible.

1. Axle Surfaces

Figure 8 presents the spectra for the right axle; each plot shows the complete set of angle measurements for a given transducer, with the downstream region in the center. The locations move outboard from PT34 (close to the strut) to PT37 (at the axle/wheel junction).

For all spanwise stations, the spectra at low frequencies (below 60 Hz) are very similar, with near-identical magnitudes within the expected wake region ($100° < \theta < 260°$) and a decrease moving around towards the upstream angles. This is consistent with the expectation of attached laminar flow in the latter area, as also are the very low levels at higher frequencies. (The localized spikes arise from electrical noise not related to the flow field. This was confirmed with reference to the wind-tunnel idle spectra.)

Above 60Hz, more distinctive spectral characteristics are evident. For PT34 and PT35, there is a broad peak from approximately 60Hz to 80Hz in the spectra around $\theta = 90°$ and $\theta = 270°$. It is also present in the spectra from the outboard transducers, but to a lesser extent. Interestingly, though, it is evident in the wake region too for these positions, whereas the PT34 and PT35 plots show it to be suppressed there.

The origin of the peak is uncertain. Although it is tempting to ascribe it to vortex shedding from the axle, the frequency is too low for plausibility. (Assuming a Strouhal number of 0.2, the axle shedding frequency would be 122Hz.) Equally, although the frequency would be possible for shedding from the strut, the locations where the peak is observed are inconsistent with this explanation. Spot checks on strut transducers have confirmed that the peak is generally absent from their spectra, with only those near PT34 and 35 in the 270° position (i.e. 3, 5 and 6)

exhibiting it. The overall conclusion, therefore, is that there is no strong evidence in the pressure spectra for coherent vortex shedding from either axle or strut.

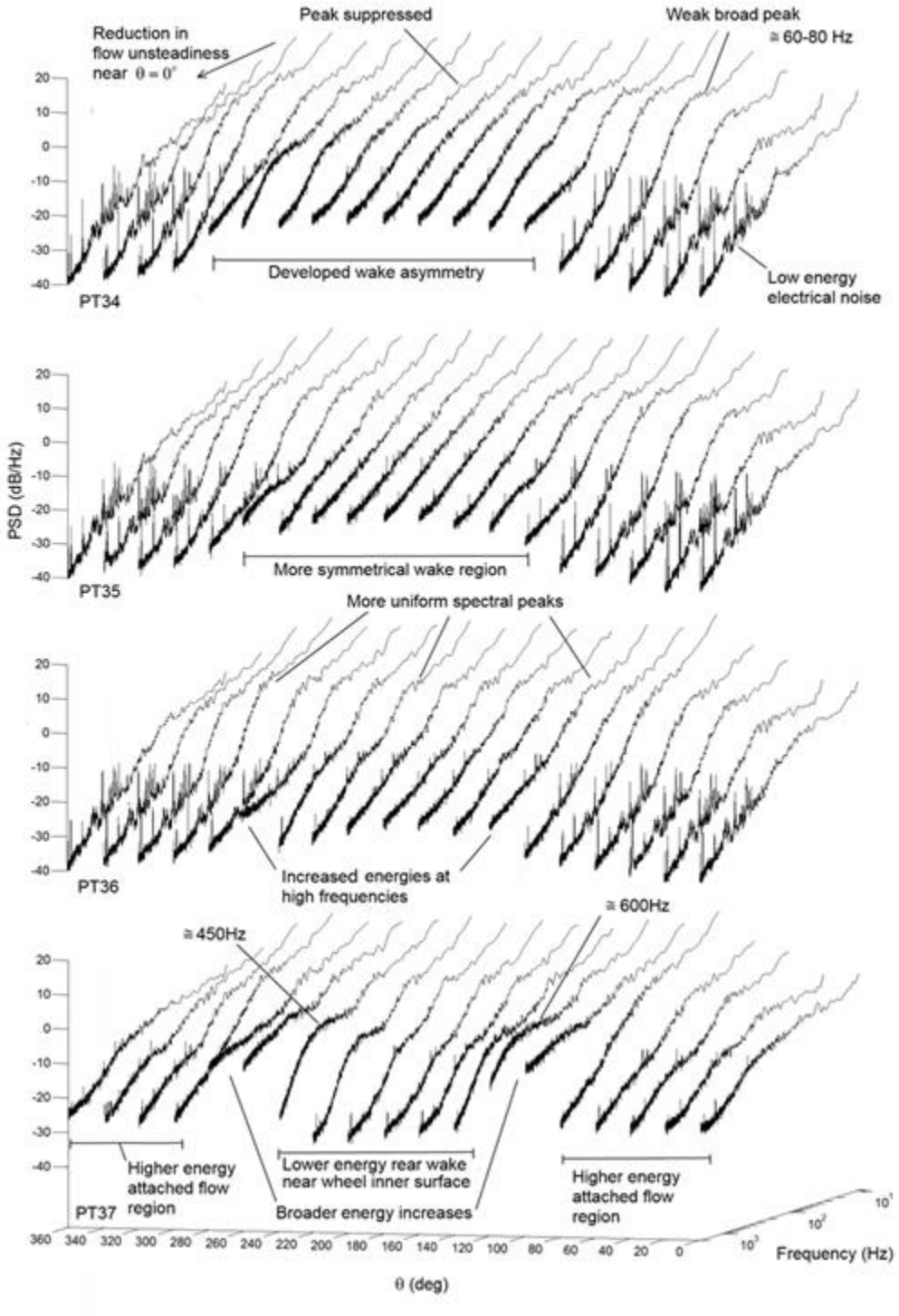

Fig. 8. Power spectral density of surface pressure over the axle.

At higher frequencies (above 500Hz), the spectral levels are heavily dependent on both spanwise and angular positions. The wake region generally has the highest values, and (with the exception of PT37, by the wheel) shows quite strong angular uniformity. Its extent is somewhat asymmetrical close to the strut (PT34), becoming less so moving outboard. The asymmetry implies later separation on the wing side, which is consistent with the attachment-line offset observed in the mean flow.

Perhaps the most interesting features of the results are evident at PT37. These spectra show isolated regions of increased high-frequency energy within the range 450-600Hz, at angles matching the shear-layer/horseshoe-vortex footprints highlighted as feature H in Fig. 7. (Initial evidence of this structure begins to show at PT36, with increases in the high-frequency energy content at 260° on the ground side and 120° on the wing side.) More generally, the effect of proximity to the wheel surface is to reduce high-frequency levels over the central wake angles, and to increase them in the upstream arc. Both observations are consistent with an oncoming boundary-layer, rather than free-stream, flow. In particular, the raised stagnation-region levels demonstrate that spectral analysis can distinguish between laminar and turbulent attached flows in a way that RMS data cannot.

Comparable data in the literature is restricted to a single spectrum from the 0° position on the LAGOON model axle [10]. High-pass filtering in these measurements attenuates components below 200Hz [9]; assuming Strouhal scaling, the equivalent frequency here is approximately 67Hz. Above this, all four transducers show a featureless, monotonically reducing, spectrum, in qualitative agreement with the LAGOON result.

2. Inboard Wheel Surfaces

Extending the analysis to the inboard wheel surface, Fig. 9 presents the spectra from PT38 (near the axle junction) to PT44 (next to the belt edge). Of these, the results for PT38 show near-identical characteristics to those already identified in Fig. 8 for its neighbor, PT37.

With an increase in radial location to PT39, two principal changes are evident. Firstly, there is a reduction in the intensity and angular separation of the peaks associated with the axle horse-shoe vortex. This is also a characteristic of the results at PT40. Both features are readily understood from the RMS results of Fig. 7; the overall unsteadiness is lower downstream, and the constant spacing of the vortex legs corresponds to reduced angle separation at larger radius.

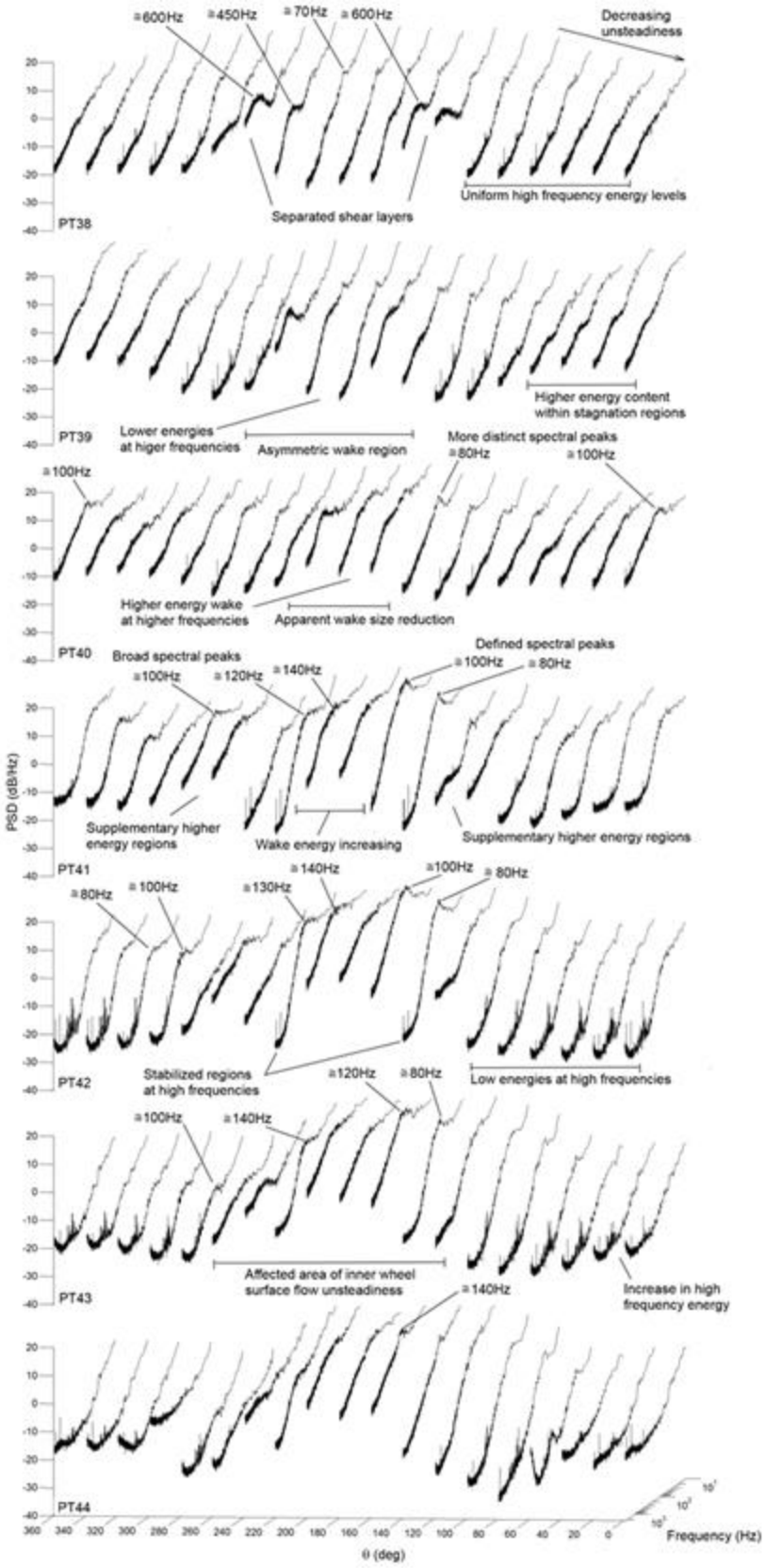

Fig. 9. PSD distributions of surface pressures over the inner right wheel surface.

The other striking alteration from PT38 to PT39 is the increase in overall levels within the upstream regions. As PT39 lies much closer to the inside edge of the shallow cavity region (see Fig. 2), and a similar increase is also evident for PT40, this can be associated with the adverse pressure gradient after the point of maximum tire width. PT40 also shows a further feature which is most likely due to that gradient: distinct spectral peaks centered around 100Hz in the 0° and 360° spectra. These are ascribed to a localized separation region formed from the inability of the flow to negotiate the sharp curvature change at the tire/hub junction. This claim is supported by the absence of similar peaks at the measurement positions either side (i.e. PT39 and PT41). In contrast, an 80Hz feature in the region $80° < \theta < 140°$ persists in recognizable form from PT39 onwards.

Another interesting difference between the results at PT39 and PT40 is the increase in spectral levels within the angular region $180° < \theta < 200°$, by around 10dB. This is interpreted as the effect of the turbulent surface flow impinging onto the initial rear portion of the tire profile (denoted by 'G' in Fig. 7). Consistent with this view is the persistence of the feature in the corresponding spectra for PT41, which is still in the impingement region.

The results for PT41 also see the development of two 'supplementary higher energy' regions located at $\theta = 100°$ and $\theta = 260°$. These imply an increase in high-frequency levels close to the outer boundary of the cavity, on both wing and ground sides. On close consideration of Fig. 7e, some evidence of this localized region of unsteadiness is evident (feature J). It appears to correspond with the expected impingement of the upstream surface flow onto the shallow cavity edge at these positions. Similar concentrated regions have been described as the development of localized regions of unsteadiness resulting from the adverse pressure gradients set up directly behind the main support strut [12]. While this is plausible for the feature on the wing side, it would not explain the existence of the one on the ground side. Furthermore, they are also, arguably at least, present in single-wheel spectra [22]. Hence they seem more likely to be simply associated with the geometry of the tire sidewall.

The supplementary higher energy regions remain clearly discernible in the spectra at maximum wheel thickness (PT42). However, high-frequency levels in the upstream arc are markedly lower, as one would expect if this aspect is determined by the streamwise pressure gradient. Wake-region levels remain high, and continue to do so as this area broadens at PT43 and PT44. These spectra also exhibit a reversion to higher levels at high frequencies in the upstream locations, presumably due to local adverse pressure gradients associated with the belt-edge corner.

3. Tire Belt Surface

The PSD results for the wheel belt are presented in Fig. 10. All positions (with the possible exception of PT50), show broadly similar characteristics. In the upstream half, the flow field exhibits a distinct lack of coherent oscillatory behavior, as well as large areas of laminarity containing very little high-frequency energy. In the downstream half, however, the higher RMS levels seen in Fig. 7 are associated with increases at all frequencies. Furthest inboard (PT45), reasonably symmetric downstream conditions are evident, and low-frequency levels are near uniform. The high frequencies, however, show a decrease (≈10dB) at $\theta = 180°$, relative to 160° and 200°. This can be interpreted as a faint remnant of the axle wake unsteadiness profile. Moving across the belt, the influence of the two inboard wheel-edge vortices identified in Fig. 5 (D and F) starts to become apparent. The impact of these vortices on overall RMS levels is manifested in Fig. 7 as regions D and E; here their effect is seen in PT47's substantially increased high-frequency energy levels at $\theta = 120°$ and $\theta = 240°$. Interestingly, though, this angular separation is much greater than would be predicted from the RMS measurements, which are dominated by lower-frequency contributions. Indeed, the latter would suggest that the vortices had become indistinguishable by PT48, whereas their spectral signatures remain clear. It thus seems that these features are associated with the flow attachment that will occur outboard of the vortex axes. They finally disappear at PT49, which shows a symmetric region of high-intensity energy at high frequencies for $120° < \theta < 240°$.

With progression to the final measurement station (PT50), adjacent to the outboard edge, there are significant and distinct changes. Firstly, there is increased evidence of flow instability, with the extent of high-frequency energy reverting back to the near-symmetric region $100° < \theta < 260°$ (cf. PT45). However, within this region high-frequency levels are up to an order of magnitude lower than for PT45, suggesting that the unsteadiness is inferior to that at the inboard rear edge. Another crucial difference is the high-frequency behavior in the upstream half. Here overall levels are significantly higher than for all other belt transducers, and well-defined spectral peaks can be observed. As will be seen, this is due to the edge separation bubble, although, surprisingly, the directly upstream position (0° and 360°) is unaffected. It is also notable that the frequency of the main spectral peak varies with angle; from about 350–450Hz on the wing side, and 400–500Hz on the ground side. At the same time it becomes less distinct, eventually merging with the broadband, as the wheel-edge flow becomes more aligned with the free-stream direction and the separation bubble disappears.

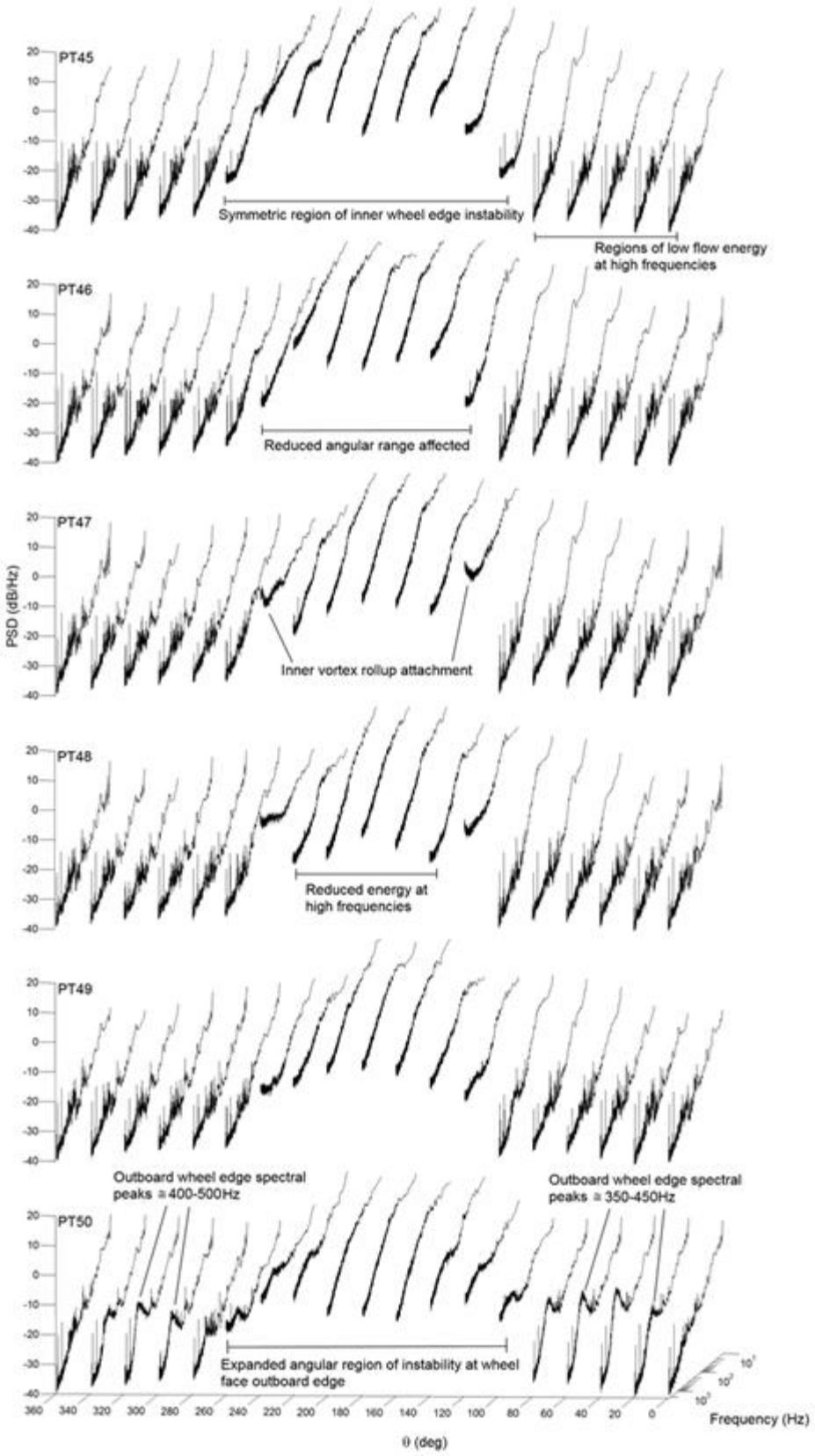

Fig. 10. PSD distributions of the surface pressures over the right wheel flat surface.

Previously reported spectra are more numerous for the tire-belt region than elsewhere, although only one of the associated studies considers the two-wheel case [10]. The relevant measurements are on the center line, and are qualitatively consistent with the results shown here, with much lower levels found in the upstream region (at θ = 300°) compared to the downstream (at θ = 180° and 220°). The latter spectra both show a smooth monotonic decrease with frequency, with no significant individual features and very similar levels. This behavior is more consistent with the current results for the off-center PT46 and PT49 than those for the central pair. If the apparent correspondence is genuine, a possible explanation is the difference in model belt widths (broader here).

The overall level increase between upstream and downstream faces is also a feature of spectra from less comparable geometries: single-wheel [22] and four-wheel [23]. Otherwise, the only notable aspect of these other results is the presence of a peak in upstream-face spectra at a Strouhal number, based on wheel diameter, of order one (equivalent to 86Hz for the current data). While it is tempting to identify a corresponding peak in Fig. 10, there is none that can genuinely be recognized as comparable. There is also none in the LAGOON spectrum at 300° [10]. Finally, given the differences in geometry and actual Strouhal value, the origins of the peaks for the single-wheel and four-wheel gears may be entirely separate. Elucidation of this issue will require further experimental effort.

4. Outboard Wheel Surfaces

To complete the spectral analysis, Fig. 11 shows the results going from the outboard edge towards the center of the outboard cavity. At PT51, the transducer lies underneath the forward-edge separation bubble for almost the entire upstream semi-circle. This is the region where the maximum mean suction is found. Overall levels here are markedly higher than for any other upstream location, with the ranges $20° < \theta < 100°$ and $260° < \theta < 340°$ showing clearly defined spectral peaks that obviously correspond to those of PT50 at the same angles. The spectacular increase in level (approximately 20dB) demonstrates how significant the difference is between attached and separated flow. This point also applies for PT52 in the upstream region, with the same peaks discernible, but at levels similar to PT50.

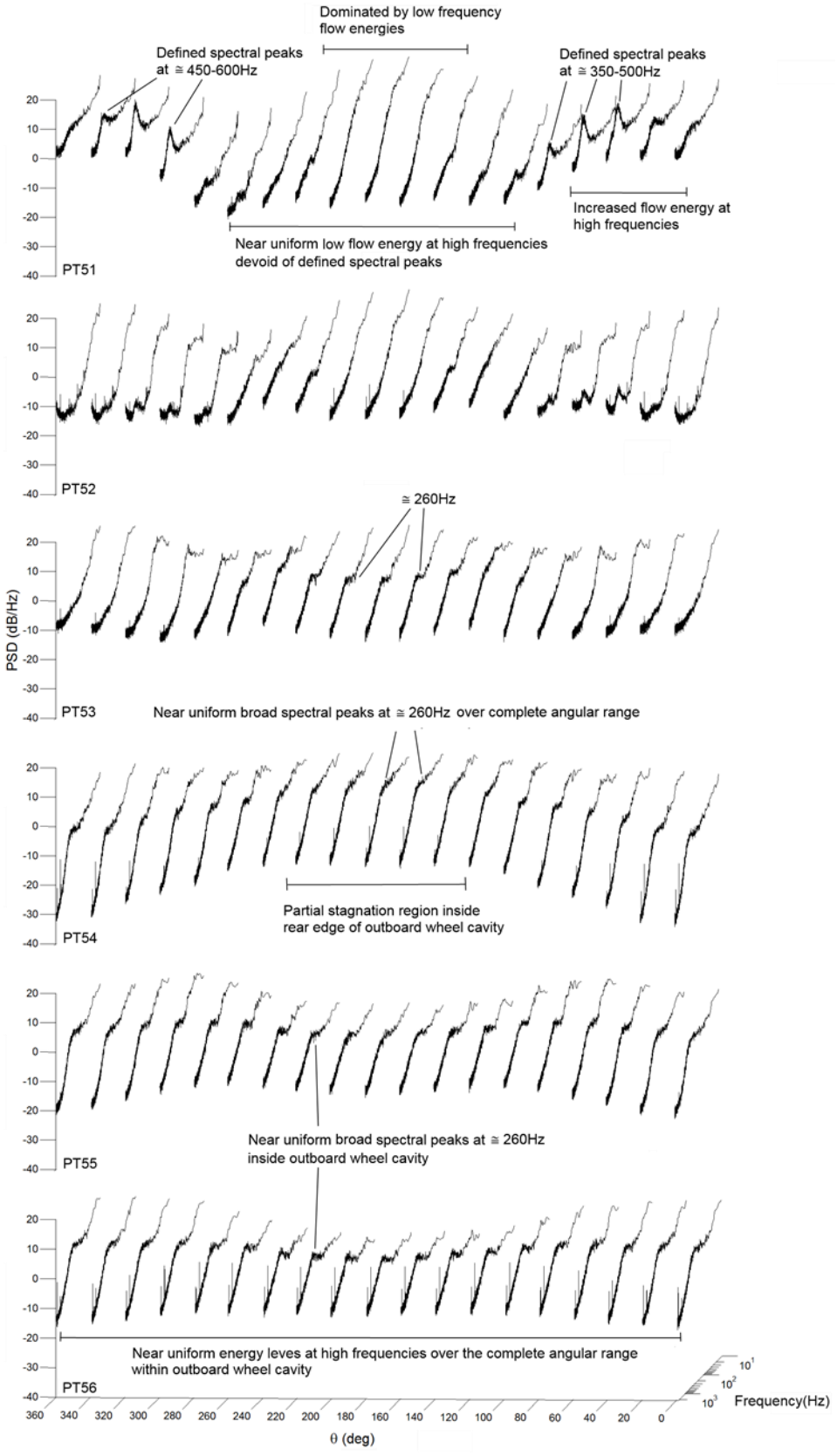

Fig. 11. PSD distributions of surface pressures over the outboard right wheel surface.

Downstream spectra for PT51 and PT52 show little structure; only as the measurements move inwards onto the sloping wall of the cavity, where flow impingement is expected, do features emerge. Thus PT53 spectra exhibit a broad spectral peak centered around 260Hz within the rear-most measurement locations, and the angular extent of this peak broadens in subsequent positions. There is also a general increase in the relative importance of the downstream region, culminating at the curvature discontinuity collocated with PT54. Further decreases in radius reveal a broadly uniform angular distribution on the flat part of the outer wheel surface.

IV. Conclusion

This paper has presented results from comprehensive surface-pressure mapping experiments on a generic, two-wheel landing-gear model without boundary-layer trips. The measurements were made possible through a novel application of low-cost transducers, combined with automated wheel/axle rotation. The upshot is a data set of unique scope and depth.

Measurements on the wheel and axle surfaces have been reported here. The analysis has proceeded from mean values, through RMS levels, to power spectral densities. Each stage has been found to provide useful information in the context of landing-gear noise, with more subtle aspects becoming evident as analysis complexity increases.

The mean-pressure data (combined with oil flow visualization) reveals the overall flow topology, confirming its well-established bluff-body characteristics: large-scale, three-dimensional separations on the wheel rear surfaces, and separation bubbles on their forward outer edges. The suppression of similar structures on the inner edges is due to the outwards deflection of the oncoming flow. This arises due to the blocking effect of the strut and axle, which also causes a secondary degree of asymmetry about the horizontal plane containing the axle.

The RMS unsteady-pressure results show that the regions of separated flow identifiable from the mean data do, as expected, have high fluctuation levels. (In the case of the forward-edge separation bubbles, these are significantly higher than seen on forced-transition models, where the bubbles are eliminated.) However, the detail variation of these levels is not straightforwardly linked to the mean pressures. Moreover, there are also areas of high RMS that are not identifiable from the mean data. The most important of these are on the wheel inner faces, adjacent to the axle wake. Elsewhere, slightly raised levels are evident on tire sidewall faces downstream of the shallow cavity formed by the hub region; these are ascribed to the impingement of flow from the cavity.

Spectral decomposition of the unsteady pressure components has the obvious benefit of extracting their frequency distribution. However, it also identifies regions of elevated high-frequency energy that are not visible from the RMS maps (because the latter are typically dominated by low-frequency contributions). Most basically, this allows differentiation between laminar and turbulent attached flows. More subtly, the latter show raised levels in areas of adverse pressure gradient. Wheel rear-surface flow impingements associated with vortical flow separations also generate such regions, offset from the vortices' traces on the RMS map. Despite their minimal impact on RMS values, the high-frequency contributions are potentially important for noise because of the frequency dependence of both far-field sound generation and human hearing sensitivity.

Finally, it should be noted that none of the spectra reported here exhibit significant tonal components. This implies not only that cavity tones are absent (unsurprisingly, given the model geometry), but also that there is no evidence of the coherent vortex shedding that is often mentioned in qualitative discussions of landing-gear noise.

In summary, the main implication of this work is that it is not sufficient to focus solely on the obvious regions of separated flow that can be inferred from steady measurements, nor even on the areas with high levels of RMS surface pressure. Spectral analysis reveals potential contributions from regions of attached turbulent flow as well. Thus the issue of transition fixing is likely to be significant even beyond its aforementioned influence on the forward-edge separation bubble. While it is clearly justifiable for CFD validation purposes, prediction of landing-gear noise in the long term could well require accurate representation of true boundary-layer states in full-scale operation.

References

[1] Dobrzynski, W., "Almost 40 years of airframe noise research: What did we achieve?," *Journal of Aircraft*, Vol. 47, No. 2, 2010, pp. 353-367.

[2] Casalino, D., Diozzi, F., Sannino, R., and Paonessa, A., "Aircraft noise reduction technologies: A bibliographic review," *Aerospace Science and Technology*, Vol. 12, 2008, pp. 1–17.

[3] Heller, H. H., and Dobrzynski, W. M., "Sound radiation from aircraft wheel-well/landing gear configurations," *Journal of Aircraft*, Vol. 14, No. 8, 1977, pp. 768-774.

[4] Dobrzynski, W., Schöning, B., Chow, L. C., Wood, C., Smith, M., and Seror, C, "Design and Testing of Low Noise Landing Gears," *International Journal of Aeroacoustics*, Vol. 5, 2006, pp. 233-262. doi: 10.1260/1475-472X.5.3.233

[5] Dobrzynski, W., Chow, L. C., Smith, M., Boillot, A., Olivier, D., and Molin, N., Experimental assessment of low noise landing gear component design, *International Journal of Aeroacoustics*, Vol. 9, 2010, pp. 763-786. doi: 10.1260/1475-472X.9.6.763

[6] Quayle P., Dowling, A, P., Babinsky, H., Graham, W. R., and Liu, Y., Mechanisms for model scale landing gear noise generation," *46th AIAA Aerospace Sciences Meeting and Exhibit*, 7-10 Jan, Reno, Nevada, 2008.

[7] Dobrzynski, W., Chow, L.C., Guion, P., and Shiells, D., "Research into landing gear airframe noise reduction," *8th AIAA/CEAS Aeroacoustics Conference & Exhibit, 2002–2409*, 17-19 June, Breckenridge/CO, 2002.

[8] Dobrzynski, W., Chow, L. C., Guion, P., and Shields, D., "A European study on landing gear airframe noise sources," *6th AIAA/CIAS Aeroacoustics conference and Exhibit*, 12-14 June, Lahaina, HI, 2000.

[9] Sanders, L., Manoha, E., Ben Khelil, S., and Francois, C., "LAGOON : CFD/CAA Coupling for Landing Gear Noise and Comparison with Experimental Database," *17th AIAA/CEAS Aeroacoustics Conference*, Portland, Oregon, 2011.

[10] De La Puente, F., Sanders, L., and Vuillot, F., "On LAGOON Nose Landing Gear CFD/CAA Computation over Unstructured Mesh using a ZDES approach," *20th AIAA/CEAS Aeroacoustics Conference*, 16-20 Jun, Atlanta, GA, 2014.

[11] Heller, H. H., and Dobrzynski, W. M., Unsteady surface pressure characteristics on aircraft components and far-field radiated airframe noise, *Journal of Aircraft*, Vol. 15, No.12, December, 1978, pp. 809-815.

[12] Lazos, B. S., "Mean flow features around the inline wheels of four-wheel landing gear," *Journal of Aircraft*, Vol. 40, No. 2, 2002, pp. 193-198.

[13] Lazos, B. S., "Surface topology on the wheels of a generic four-wheel landing gear," *Journal of Aircraft*, Vol. 40, No. 2, 2002, pp. 2402-2411.

[14] Manoha, E., Bulté, J., and Caruelle, B., "LAGOON : an Experimental Database for the Validation of CFD/CAA Methods for Landing Gear Noise Prediction", *14th AIAA/CEAS Aeroacoustics Conference*, 5-7 May, Vancouver, Canada, 2008.

[15] Manoha, E., Bulté, J., Ciobaca, V., and Caruelle, B., "LAGOON : further analysis of aerodynamic experiments and early aeroacoustics results," *15th AIAA/CEAS Aeroacoustics Conference*, 12-14 May, Miami, Florida, 2009.

[16] Sanders, L., Manoha, E., Ben Khelil, S., and Francois, C., "LAGOON: New Mach Landing Gear Noise Computation and further analysis of the CAA process," *18th AIAA/CEAS Aeroacoustics Conference*, Colorado Springs, CO, 2012.

[17] Sanders, L., Manoha, E., Ben Khelil, S., and François, C., "CFD/CAA coupling on the LAGOON #2 landing gear using a structured multi-block solver with the Chimera technique," *19th AIAA/CEAS Aeroacoustics Conference*, 27-29 May, Berlin, Germany, 2013.

[18] Liu, W., Kim, J. W., Zhang, X., Angland, D., and Caruelle, B., "Landing-gear noise prediction using high-order finite difference schemes," *Journal of Sound and Vibration*, Vol. 332, 2013, pp. 3517-3534.

[19] Imamura, T., Hirai, T., Amemiya, K., Yokokawa, Y., Enomoto, S., and Yamamoto, K., "Aerodynamic and aeroacoustic simulations of a two-wheel landing gear," *Procedia Engineering*, Vol. 6, 2010, pp. 293-302.

[20] Venkatakrishnan, L., Karthikeyan, N., and Mejia, K., "Experimental Studies on a Rudimentary Four-Wheel landing Gear," *AIAA Journal*, Vol. 50, No. 11, 2012, pp. 2435-2447. doi: 10.2514/1.J051639.

[21] Spalart, P. R., and Mejia, K. M., "Analysis of Experimental and Numerical Studies of the Rudimentary Landing Gear," *49th AIAA Aerospace Sciences meeting including the new horizons forum and aerospace exposition*, 4-7 Jan, Orlando, Florida, 2011.

[22] Zhang, X., Ma, Z., Smith, M. and Sanderson, M., "Aerodynamic and acoustic measurements of a single landing gear wheel," *19th AIAA/CEAS Aeroacoustics Conference*. 27-29 May, Berlin, Germany, 2013.

[23] Xiao, Z., Liu, J., Luo, K., Huang, J., and Fu, S., "Investigation of flows around a rudimentary landing gear with advanced detached-eddy-simulation approaches," *AIAA Journal*, Vol. 51, No. 1, 2013, pp. 107-125.